Current $CaCO_3$ dissolution at the seafloor caused by anthropogenic CO_2

Olivier Sulpis[a,b,1], Bernard P. Boudreau[c], Alfonso Mucci[a,b], Chris Jenkins[d], David S. Trossman[e], Brian K. Arbic[f], and Robert M. Key[g]

[a]GEOTOP, McGill University, Montreal, QC H3A 0E8, Canada; [b]Department of Earth and Planetary Sciences, McGill University, Montreal, QC H3A 0E8, Canada; [c]Department of Oceanography, Dalhousie University, Halifax, NS B3H 4R2, Canada; [d]Institute for Arctic and Alpine Research, University of Colorado at Boulder, Boulder, CO 80309-0450; [e]Institute of Computational Engineering and Sciences, The University of Texas at Austin, Austin, TX 78712-1229; [f]Department of Earth and Environmental Sciences, University of Michigan, Ann Arbor, MI 48109-1005; and [g]Atmospheric and Oceanic Sciences, Princeton University, Princeton, NJ 08540-6654

Edited by Donald E. Canfield, Institute of Biology and Nordic Center for Earth Evolution, University of Southern Denmark, Odense M., Denmark, and approved September 25, 2018 (received for review March 10, 2018)

Oceanic uptake of anthropogenic CO_2 leads to decreased pH, carbonate ion concentration, and saturation state with respect to $CaCO_3$ minerals, causing increased dissolution of these minerals at the deep seafloor. This additional dissolution will figure prominently in the neutralization of man-made CO_2. However, there has been no concerted assessment of the current extent of anthropogenic $CaCO_3$ dissolution at the deep seafloor. Here, recent databases of bottom-water chemistry, benthic currents, and $CaCO_3$ content of deep-sea sediments are combined with a rate model to derive the global distribution of benthic calcite dissolution rates and obtain primary confirmation of an anthropogenic component. By comparing preindustrial with present-day rates, we determine that significant anthropogenic dissolution now occurs in the western North Atlantic, amounting to 40–100% of the total seafloor dissolution at its most intense locations. At these locations, the calcite compensation depth has risen ∼300 m. Increased benthic dissolution was also revealed at various hot spots in the southern extent of the Atlantic, Indian, and Pacific Oceans. Our findings place constraints on future predictions of ocean acidification, are consequential to the fate of benthic calcifiers, and indicate that a by-product of human activities is currently altering the geological record of the deep sea.

ocean acidification | seafloor | $CaCO_3$ | dissolution | anthropogenic CO_2

Seafloor dissolution of $CaCO_3$ minerals will constitute a primary feedback to ocean acidification over timescales of centuries to tens of millennia (1). The overall dissolution reaction is as follows:

$$CaCO_3 + CO_2 + H_2O \rightarrow Ca^{2+} + 2\,HCO_3^-, \qquad [1]$$

where $CaCO_3$ denotes solid carbonate in bottom sediments, mainly as calcite. This process is termed geochemical carbonate compensation. Consequently, CO_2 entering the ocean, including that of anthropogenic origin, can be neutralized permanently by conversion to dissolved bicarbonate ions (HCO_3^-).

The upper oceans are wholly supersaturated with respect to calcite, despite the current acidification. Largely because of the increasing solubility of calcite with pressure, the deeper oceans become undersaturated, whereafter the rate of reaction **1** increases with oceanographic depth. The depth where undersaturation first occurs is the calcite saturation depth (CSD) (2). The preindustrial oceans contained CO_2 acquired from the atmosphere, from marine volcanism, and from oxic organic matter decay. At the same time, calcifying organisms precipitated $CaCO_3$ shells that settled to the seafloor upon their death. Combined, these processes and reaction **1** lead to decreasing $CaCO_3$ content in sediments below the CSD. The depth where the deposition rate of $CaCO_3$ is exactly balanced by reaction **1** is called the calcite compensation depth (CCD) (2), although operationally it is commonly defined as the depth where the sediment $CaCO_3$ content falls below 10%. The snowline (2) denotes the depth below which no $CaCO_3$ is found in the sediment; the snowline and CCD coincide at steady state (2).

The geological record contains numerous examples of deep-sea $CaCO_3$ dissolution events driven by natural acidification, for example, at ∼56 My BP, known as the Paleocene–Eocene Thermal Maximum (3–5). During these events, $CaCO_3$ disappeared from deep-sea sediments, where it had previously accumulated, burial rates dropped, and the snowline shoaled. The same scenario has been predicted for the Anthropocene oceans (6, 7), but no estimates of increased deep-sea sediment $CaCO_3$ dissolution have been published. This lack of documentation might be attributed to the restricted penetration of anthropogenic CO_2 to shallow depths, but this premise is contradicted by observed changes in the carbonate chemistry of the deeper oceans (8–10) and as reported here. Both numerical ocean models and the presence in abyssal waters of transient tracers produced almost entirely after the end of the 1940s, that is, chlorofluorocarbons and polychlorinated biphenyls, strongly imply the presence of anthropogenic CO_2 in the deep oceans. Anthropogenic CO_2 in deep and bottom waters is simply very difficult to measure because it is a small signal superimposed on a large natural background concentration. Early changes in

Significance

The geological record contains numerous examples of "greenhouse periods" and ocean acidification episodes, where the spreading of corrosive (CO_2-enriched) bottom waters enhances the dissolution of $CaCO_3$ minerals delivered to the seafloor or contained within deep-sea sediments. The dissolution of sedimentary $CaCO_3$ neutralizes excess CO_2, thus preventing runaway acidification, and acts as a negative-feedback mechanism in regulating atmospheric CO_2 levels over timescales of centuries to millennia. We report an observation-based indication and quantification of significant $CaCO_3$ dissolution at the seafloor caused by man-made CO_2. This dissolution is already occurring at various locations in the deep ocean, particularly in the northern Atlantic and near the Southern Ocean, where the bottom waters are young and rich in anthropogenic CO_2.

Author contributions: O.S., B.P.B., and A.M. designed research; O.S. performed research; O.S., B.P.B., A.M., C.J., D.S.T., B.K.A., and R.M.K. contributed new reagents/analytic tools; O.S., B.P.B., C.J., D.S.T., B.K.A., and R.M.K. analyzed data; and O.S., B.P.B., A.M., C.J., D.S.T., B.K.A., and R.M.K. wrote the paper.

The authors declare no conflict of interest.

This article is a PNAS Direct Submission.

[1]To whom correspondence should be addressed. Email: olivier.sulpis@mail.mcgill.ca.

This article contains supporting information online at www.pnas.org/lookup/suppl/doi:10.1073/pnas.1804250115/-/DCSupplemental.

Published online October 29, 2018.

$CaCO_3$ content of sediments caused by anthropogenic acidification are also extremely difficult to detect through changes in either solid mass or dissolution indices.

Given that sediment monitoring is unlikely to yield immediate evidence of anthropogenic calcite dissolution at the seafloor, we employ a different approach and compare the rate of dissolution at the seafloor under preindustrial (~1800 AD) and modern (2002 AD) benthic conditions. In accord with recent work (11, 12) on the dissolution kinetics of calcite beds, the dissolution rate (r) at any depth between the CSD and the CCD is given by the following (11):

$$r = k^*\left([CO_3^{2-}]_{eq} - [CO_3^{2-}]_{SW}\right), \quad [2]$$

where $[CO_3^{2-}]_{eq}$ is the calcite-equilibrium carbonate ion concentration (Fig. 1*B*), $[CO_3^{2-}]_{SW}$ is the carbonate ion concentration in bottom waters, and k^* is the overall CO_3^{2-} mass transfer coefficient (11):

$$k^* = k_s\beta(k_s + \beta)^{-1}, \quad [3]$$

where k_s is the sediment-side mass transfer coefficient, which characterizes dissolution and transport (diffusion) of the carbonate ion within the sediment, and β is the water-side mass transfer coefficient (13). In this formulation, k^* tends toward the value of the smallest rate-limiting mass transfer coefficient, β or k_S, without ever reaching it, as predicted by theory and validated by observations. For further explanation with regard to the derivation of Eqs. **2** and **3**, please see *SI Appendix*.

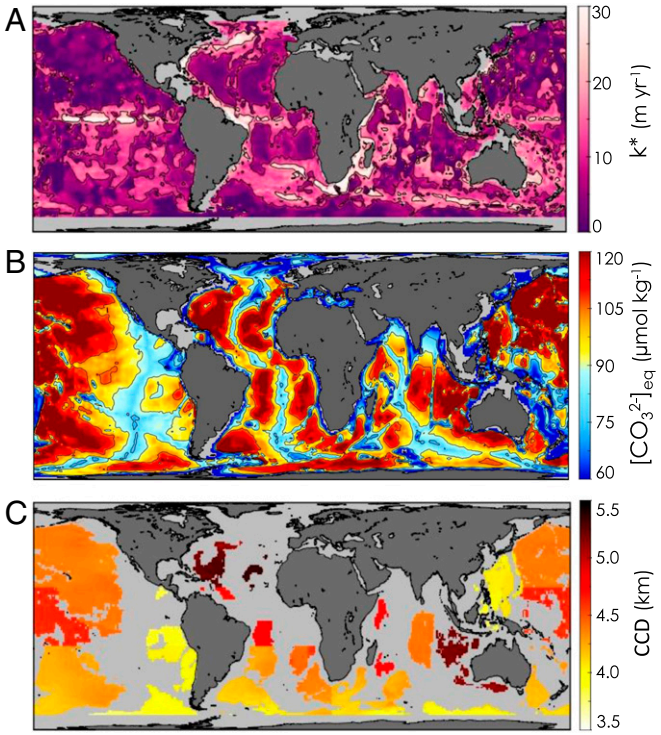

Fig. 1. Chemical and physical parameters for calcite dissolution. (*A*) Overall mass transfer coefficient k^* for $CaCO_3$ dissolution, (*B*) current bottom-water saturation concentration $[CO_3^{2-}]_{eq}$ at in situ temperature, salinity, and pressure, and (*C*) present-day calcite compensation depth (CCD), regionally averaged as described in *Materials and Methods*, where the light gray identifies areas where the CCD is deeper than the depth of the seafloor, that is, where calcite can undergo net sediment accumulation. The CCD is not computed in the Arctic and Southern Oceans (south of 60°S).

With any Anthropocene (14) rise in the CCD, r is supplemented by dissolution of previously deposited $CaCO_3$ between the new and old CCD positions (*Materials and Methods*). Hence, the difference between the calculated r over the deep seafloor for preindustrial and current conditions reflects the impacts of anthropogenic acidification. To perform this calculation globally, we require the spatial distributions of k^*, $[CO_3^{2-}]_{eq}$, $[CO_3^{2-}]_{SW}$, and the $CaCO_3$ contents of surface sediments, whose distribution is available from a new database (15, 16) and displayed in *SI Appendix*, Fig. S2*A*.

The distribution of k^* at the seafloor is shown in Fig. 1*A*. The water-side mass transfer coefficient, β, appears in Eq. **3** because the seafloor is covered by a water layer through which solute transport occurs via molecular diffusion (13), termed the diffusive boundary layer (DBL). The existence of the DBL has been amply illustrated by previous research (17–19). β is calculated as the ratio of the diffusion coefficient of CO_3^{2-} ($D_{CO_3^{2-}}$), at in situ temperature (T) and salinity (S_P), to the thickness of the DBL (Z_{DBL}), as β is effectively independent of pressure (*Materials and Methods*). Whereas $D_{CO_3^{2-}}$ does not vary widely, Z_{DBL} depends on the flow velocities at the seafloor (13), but an ocean-wide distribution of Z_{DBL} has never been reported in the literature. Herein, we use a global bottom-current velocity (U) model to derive in situ β values (*Materials and Methods*). *SI Appendix*, Fig. S3*C* provides an ocean-wide distribution of β and shows that this parameter is high on the east side of continents, beneath the Equator, and on the northern fringe of the Southern Ocean, all areas with enhanced bottom currents. Conversely, β is very small over much of the abyssal ocean due to relatively sluggish flow. The magnitude of k_s is derived from available experiments and calculated as a function of the $CaCO_3$ content in surface sediments (*Materials and Methods*). The distribution of k_s at the seafloor is shown in *SI Appendix*, Fig. S2*B*. Overall, the rate of deep-sea $CaCO_3$ dissolution, r, is largely controlled by β, rather than k_s (11, 12), except in regions of high bottom currents or where sediments are $CaCO_3$-poor, such as the North Pacific or the Southern Ocean (*SI Appendix*, Fig. S5).

The benthic distribution of $[CO_3^{2-}]_{eq}$ in Eq. **2** is calculated by dividing the stoichiometric solubility constant of calcite, K^*_{sp}, at in situ conditions, by the Ca^{2+} concentration of the oceans. Fig. 1*B* illustrates the resulting map of $[CO_3^{2-}]_{eq}$. $[CO_3^{2-}]_{eq}$ is commonly near 75 μmol·kg^{-1} on top of oceanic ridges (~2,500 m) but increases to values as high as ~140 μmol·kg^{-1} on the abyssal plains (~6,000 m).

Next, we need to estimate the position of the preindustrial CCD to calculate the amount of dissolution below this depth. As stated earlier, the CCD and snowline are coincident at oceanic steady state. In addition, there is no evidence that the calcite snowline has, as yet, migrated measurably due to anthropogenic dissolution (7, 20). Therefore, we set the preindustrial CCD to the current snowline depth that we estimate from the $CaCO_3$ contents of sediments for each basin (*Materials and Methods*). With these local preindustrial CCD values, the flux (F) of $CaCO_3$ at that depth, and corresponding grid point, can be estimated (2), and the dissolution rate below the CCD, set to the value of F, mapped.

We note that calcifying organisms exhibit various responses to elevated pCO_2 conditions, due to the influence of other climate change-related effects, such as the warming of waters that counteracts acidification (21–24). In the absence of unequivocal evidence of an immediate increase or decrease in the total calcification rate in the pelagic oceans, we assume that the flux of calcitic particles reaching the CCD (F) has remained invariant since the preindustrial era. This is supported by what took place in similar acidification events in the geological record, such as the Paleocene–Eocene Thermal Maximum, where no obvious plankton carbonate productivity reduction is readily detectable (25). Thus, the "current" CCD was computed from the fixed (known) F and the present-day $[CO_3^{2-}]_{SW}$, and is represented in Fig. 1*C*.

Finally, the preindustrial distribution of bottom-water $[CO_3^{2-}]_{SW}$ (Fig. 2*A*) is computed using estimated preindustrial, deep-ocean

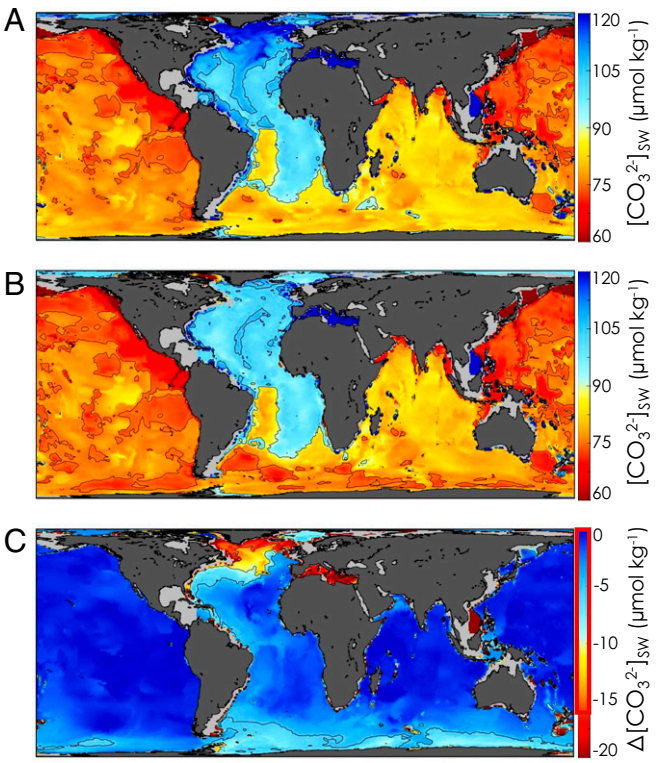

Fig. 2. Ocean acidification and bottom-water $[CO_3^{2-}]_{SW}$ decrease. (*A*) Preindustrial bottom-water $[CO_3^{2-}]_{SW}$, (*B*) current bottom-water $[CO_3^{2-}]_{SW}$, and (*C*) difference between preindustrial and current bottom-water $[CO_3^{2-}]_{SW}$ ($\Delta[CO_3^{2-}]_{SW}$ = current bottom-water $[CO_3^{2-}]_{SW}$ − preindustrial bottom-water $[CO_3^{2-}]_{SW}$), below 300 m. Uncertainties are indicated by the red outline on the color bar, corresponding to 1 SD of 16.9 μmol·kg^{-1} for $\Delta[CO_3^{2-}]_{SW}$.

dissolved inorganic carbon (DIC) concentrations (26) and the present-day total alkalinity (TA), which is assumed to have remained invariant so far over the Anthropocene (*Materials and Methods*). The current bottom-water $[CO_3^{2-}]_{SW}$ is estimated from the DIC, normalized to the calendar year 2002 (26) (Fig. 2*B*). The anthropogenic decrease of bottom-water $[CO_3^{2-}]_{SW}$ is currently limited mostly to the northern Atlantic Ocean and the Southern Ocean, where surface waters enter the deep-ocean reservoir (27). Accordingly, North Atlantic $[CO_3^{2-}]_{SW}$ has decreased from ∼110 to ∼95 μmol·kg^{-1}, whereas the North Pacific $[CO_3^{2-}]_{SW}$ has remained approximately constant at ∼70 μmol·kg^{-1}. The difference between the preindustrial and current bottom-water $[CO_3^{2-}]_{SW}$ is illustrated in Fig. 2*C*, which highlights areas of deep acidification in the northwestern North Atlantic and Southern Ocean.

Results

With the above information, we calculated the distribution of both preindustrial (Fig. 3*A*) and current (Fig. 3*B*) calcite dissolution rates at the seafloor. In both figures, areas with low k^* values (Fig. 1*A*), such as the abyssal plains on each side of the North Atlantic midocean ridge or in the North Pacific, are typified by low calcite dissolution rates, whereas sediments subject to faster currents (larger β values) or rich in $CaCO_3$ (larger k_S values) exhibit greater rates. The difference between current and preindustrial calcite dissolution rates, as plotted in Fig. 3*C*, corresponds to the rate of anthropogenic calcite dissolution at the seafloor. The anthropogenic dissolution is most pronounced and widespread in the northwestern Atlantic Ocean. There are also areas of significant dissolution in the southern Atlantic and Indian Oceans, resulting from the presence of tangible anthropogenic CO_2 in these deep waters (9, 26), and a consequent rise in the CSD. These prominent dissolution areas reflect the loci of anthropogenic CO_2 introduction into the deep oceans (North Atlantic and the Antarctic margins) and/or the presence of faster bottom currents (larger β values). In the "hot" area of the northwest Atlantic, the anthropogenic component now accounts for 40–100% of the total dissolution rate.

The seafloor area between the current and the preindustrial CCD contains the calcitic sediments subjected to the greatest increase in their dissolution rate. In this fringe of high-end anthropogenic dissolution, the $CaCO_3$ budget at the sediment–water interface (SWI) switches from gain (net accumulation) to deficit (net depletion) when the rising CCD becomes shallower than the seafloor, causing the dissolution of falling calcitic particles before their burial in the sediment. Fig. 3*C* also suggests the existence of numerous small "hot spots" of dissolution in the Indian and Pacific Oceans, corresponding to topographic highs or islands, for example, Guam and Pitcairn Islands, where the CCD has risen above the seafloor.

Because of anthropogenic CO_2 uptake by the oceans, both the saturation (CSD) and compensation (CCD) depths should shoal, leading to dissolution of previously deposited carbonate minerals (28), also known as chemical burndown. Fig. 4 presents our estimates of the upward displacements of the CSD and CCD to date for the Atlantic, plotted with the regionally averaged surface-sediment calcite content water-depth profiles (see *SI Appendix*, Table S1 for other basins). These results constitute strong signs of anthropogenic dissolution just below the current (risen) CSD, illustrating dissolution of previously deposited calcite, in particular in the North Atlantic where shoaling of the CSD and CCD is greatest.

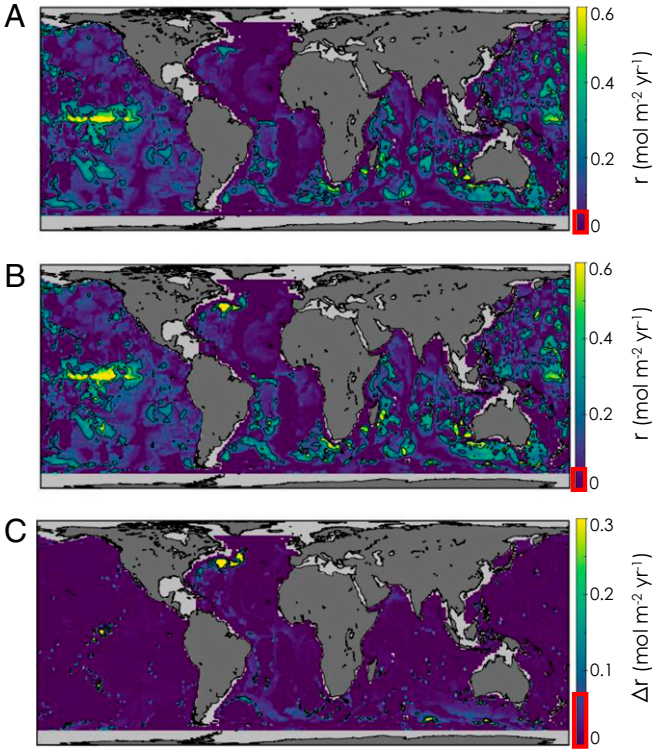

Fig. 3. Geographic calcite dissolution rate distribution and anthropogenic impact. (*A*) Preindustrial and (*B*) current calcite dissolution rate (r) at the SWI, and (*C*) the difference between preindustrial and current calcite dissolution rate below 300 m (Δr = current r − preindustrial r), that is, the anthropogenic CO_2-driven calcite dissolution rate. Hence, this excludes possible calcite dissolution on the continental shelves, particularly in the North Pacific, where the CCD shoals to less than 300 m. Uncertainties are indicated by the red outline on the color bars, corresponding to the SD, equal to 0.05 mol·m·y^{-1} for r and to 0.07 mol·m·y^{-1} for Δr.

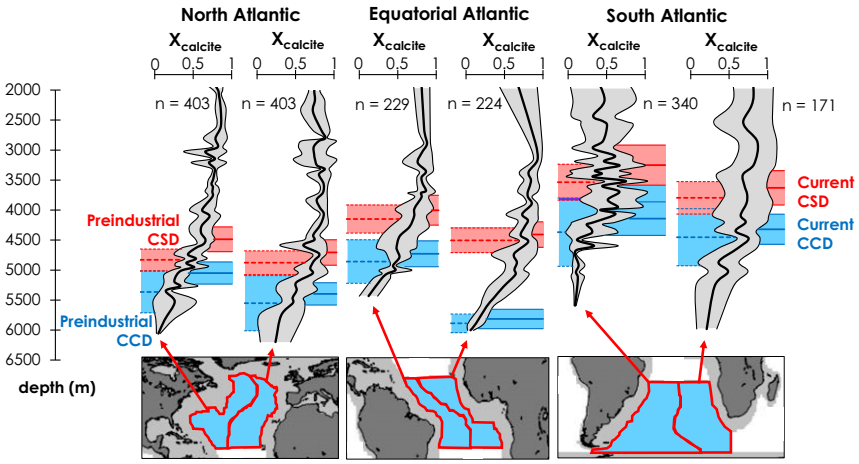

Fig. 4. Atlantic Ocean sediment calcite content profiles and calcite marker horizons. Calcite fraction in dry sediments ($X_{calcite}$), ±1 SD, for the basins defined by the maps below the plots. The number of measurements (*n*) comprised within each basin is also reported. The preindustrial calcite compensation depth (CCD) and saturation depth (CSD) are represented with dashed horizontal lines (on the *Left* of each profile), whereas the solid horizontal lines correspond to current values (on the *Right* of each profile). Both the CCD and CSD are reported along with their uncertainties.

Discussion

On average, we find that *F*, the flux of $CaCO_3$ that must reach the CCD to explain the observed $CaCO_3$ contents in surficial sediments (*Materials and Methods*) is 0.17 ± 0.07 mol·m^{-2}·y^{-1}. This value is equivalent to $CaCO_3$ fluxes to the deep ocean derived from previous studies based on excess total alkalinity (TA*) budgets (29, 30). Integrating over the surface of the seafloor, we find a global calcite downward flux at the CCD of 54 ± 17 × 10^{12} mol·y^{-1} (i.e., 0.7 ± 0.2 Gt C·y^{-1}), and a current global seafloor $CaCO_3$ dissolution flux of 32 ± 12 × 10^{12} mol·y^{-1} of $CaCO_3$ (i.e., 0.4 ± 0.1 Gt C·y^{-1}). Both of these values are similar to and more precise than the observation-based estimates presented in ref. 29. Our global dissolution estimate represents only 22 ± 8% of the total estimated $CaCO_3$ dissolution in the marine environment each year, that is, 144 × 10^{12} mol·y^{-1}, or 1.7 Gt C·y^{-1} (31). The remainder of the dissolution occurs primarily in the water column and, possibly, after burial through metabolic dissolution or later diagenesis at shallow to mid depths.

As stated and justified earlier, we assumed that the calcite rain rate has remained invariant since preindustrial times. Although a decrease in the precipitation rate of calcite might be expected under more acidic conditions (32), thus reducing the calcite export from the surface ocean and the rain rate to deep-sea sediments, no such trend is clearly observed today (33). Testing the sensitivity of the computed sediment dissolution rates (*r*) to a reduction in the calcite downward flux (*F*), we find that when *F* is decreased by 10%, the global dissolution rate increases by 2.5%. Likewise, when *F* is decreased by 20%, the global dissolution rate increases by 3.1%. Thus, counterintuitively, if less calcite is currently delivered to the seafloor than during the preindustrial era, more calcite is being dissolved at the SWI because a weaker *F* causes the CCD to respond faster to changes in $[CO_3^{2-}]_{SW}$, as explained in ref. 2, and in the case of the present acidification, to rise faster. Sediments that were above the preindustrial CCD and are now below the current CCD are subject to the greatest dissolution rate increase, as can be seen when comparing Eqs. **12–14** in *Materials and Methods*. In other words, if *F* has remained constant, ∼2% of the seafloor is currently comprised between the preindustrial and current CCD, but this fraction increases to 9.3% when *F* is reduced by 20% relative to its preindustrial value.

Our results provide a tangible indication that significant anthropogenic calcite dissolution is currently occurring at the seafloor. This dissolution will eventually change the $CaCO_3$ accumulation patterns and rates in the oceans, while mitigating runaway ocean acidification. Any future model of oceanic acidification needs to reproduce our observations to assure its validity. The consequences of this anthropogenic dissolution to the ecology of benthic calcifiers has not been determined with certainty, but could be as substantial as it is for pelagic calcifiers (34). Chemical burndown of previously deposited carbonate-rich sediments has already begun and will intensify and spread over vast areas of the seafloor during the next decades and centuries, thus altering the geological record of the deep sea. The deep-sea benthic environment, which covers ∼60% of our planet, has indeed entered the Anthropocene.

Materials and Methods

Bottom-Water Chemistry. $[CO_3^{2-}]_{SW}$ values were computed using the Matlab version of the CO2SYS program (35, 36), based on GLODAPv2.2016b 1° × 1° global mapped climatologies (13, 37) at the deepest resolved layers of the GLODAPv2.2016b model (shown in *SI Appendix*, Fig. S1), assumed to be near the seafloor. The GLODAPv2.2016b variables used for our computation are represented in *SI Appendix*, Fig. S1 and include in situ bottom-water TA, DIC, *T*, S_P, as well as soluble reactive phosphate ([SRP]) and dissolved inorganic silica ([DSi]) concentrations. Current $[CO_3^{2-}]_{SW}$ were derived using GLODAPv2.2016b bottom-water DIC data normalized to the year 2002 (*SI Appendix*, Fig. S1*G*), whereas preindustrial $[CO_3^{2-}]_{SW}$ values were computed using the GLODAPv2.2016b bottom-water preindustrial DIC data (13) (*SI Appendix*, Fig. S1*H*). For computational purposes, we assume that bottom-water TA has not changed since the end of the preindustrial period (∼1800 AD), in accordance with recent studies that predict an insignificant global mean deep-water TA anomaly (ΔTA ∼2.5 μmol·kg^{-1} relative to the mean concentration from 1950 to 1959) before ∼2060 AD, although some changes might already be detectable (during the 2010–2020 decade) in the deep North Atlantic (38). We computed the TA flux generated by anthropogenic dissolution of $CaCO_3$ sediments since the preindustrial times. Assuming that this TA mixes in the water column up to the permanent thermocline, we found that it has resulted in a world-averaged TA increase of less than 0.1 μmol·kg^{-1}, and of ∼3 μmol·kg^{-1} above the hot spot of anthropogenic dissolution in the Northwest Atlantic; both values are at or below the current analytical uncertainty. $[CO_3^{2-}]_{eq}$ was estimated from the equations presented in ref. 2, using $[Ca^{2+}]$ computed from S_P following ref. 39, the stoichiometric solubility product of calcite (K_{sp}*) (40) at in situ *T* and S_P, and the pressure (*P*) derived from GEBCO bathymetry (41).

$CaCO_3$ Distribution in Deep-Sea Sediments. The data (*SI Appendix*, Fig. S2*A*) on carbonate mineral sediment contents are composed of 1.7 million sites throughout the world's ocean, extracted from the comprehensive database of seabed sediment properties, dbSEABED (15). The original data are quality controlled and harmonized (16) so that analytical results and descriptions can be combined into a statistically homogeneous set of values. The sites are located geographically and by water depth. The surficial 0- to 10-cm (occasionally 0- to 30-cm) average values were used to compile the maps, a depth that takes account of scales of seafloor–seawater contact, including the effects of erosion and bioturbation.

Water-Side CO_3^{2-} Mass Transfer Coefficient (β). The DBL thickness (Z_{DBL}) at the air–sea interface is commonly derived from wind speed (42). In analogy, we describe a set of equations to estimate the benthic Z_{DBL} and the CO_3^{2-} water-side mass transfer coefficient (β) at in situ *T* and S_P, using the horizontal current speed (*U*) near the seafloor. In this study, we consider β to be independent of pressure, as the pressure effect on the viscosity of seawater and on the diffusion coefficients of ions in seawater is thought to be relatively small, that is, at most 8% (43). We use an interpolated version of horizontal bottom-water current speeds at 1° × 1° resolution from a higher resolution model (*SI Appendix*, Fig.

S3A). The bottom currents were inferred from an inline computation of the annually averaged kinetic energy field of a nominally 1/25th degree global configuration of the hybrid coordinate ocean model (HYCOM). It accounts for topographic internal lee wave drag, forced by air–sea fluxes and winds from reanalysis, but does not include tides (44). Neglecting tides is a source of uncertainty in this study, and this should be examined in future research. Nevertheless, abyssal tidal velocities (typically about 1 cm·s^{-1}) (45) are very likely to be smaller than nontidal velocities over most areas studied in this paper (*SI Appendix*, Fig. S3*A*). For a discussion of the sensitivity of our dissolution rate model to various initial kinetic energy distribution models, please see *SI Appendix*. Herein, for the sake of brevity, we refer to the current "speed" (a scalar) as current "velocity" (a vector), although our model does not use or require any information about the direction of the current. We assume (*i*) that these current velocities, averaged over the bottom 500 m, are representative of the current velocities just above the bottom boundary layer, that is, portions of sediment and water column affected directly in the distribution of their properties and processes by the presence of the SWI (13), comprising, among others, the DBL, (*ii*) that the seafloor is hydrodynamically smooth, and (*iii*) that there is no vertical density gradient, that is, the bottom boundary layer is unstratified.

Using the universal logarithmic velocity distribution, we then have the following:

$$\frac{u(z)}{u^*}=\frac{1}{\kappa}\ln\left(\frac{zu^*}{\nu}\right)+C, \quad [4]$$

where z is the height above the bottom, κ is the dimensionless von Karman constant (0.40) from ref. 46, ν is the molecular kinematic viscosity of seawater at $S_P = 35$ and in situ T, and C is an empirical dimensionless constant with a value of 5.1, taken from ref. 46.

The current velocity U at the upper edge of the bottom boundary layer is assumed to be equal to the current velocity averaged over the bottom 500 m and is then given by the following:

$$U=\frac{u^*}{\kappa}\ln\left(\frac{\delta u^*}{\nu}\right)+Cu^*, \quad [5]$$

where δ is the bottom boundary layer thickness.

We further assume that δ corresponds to the so-called Ekman scale height (13), reflecting classical Ekman dynamics, in which the height of the bottom boundary layer is limited by the Earth's rotation:

$$\delta=\frac{\kappa u^*}{f}, \quad [6]$$

where f is the Coriolis parameter (set to 1×10^{-4} s^{-1}). We consider a constant S_P of 35, due to the small variations of this variable in oceanic bottom waters, as shown in *SI Appendix*, Fig. S1*C*.

Combining Eqs. **5** and **6**, we obtain the following:

$$U=\frac{u^*}{\kappa}\ln\left(\frac{\kappa u^{*2}}{f\nu}\right)+Cu^*. \quad [7]$$

Fitting a power function that relates u^* to U, for $T = 2$ °C, with $R^2 > 0.999$, we have that

$$u^*=0.023U^{0.84}. \quad [8]$$

This equation gives u^* values that are notably similar to previously published empirical relationships (47, 48), for example, $u^* = U/30$, as shown in *SI Appendix*, Fig. S4*A*.

The mass transfer coefficient, β, can be found for the carbonate ion (CO_3^{2-}) following ref. 49 and u^* from Eq. **8**:

$$\beta=0.0417u^*Sc^{-2/3}, \quad [9]$$

where Sc is the Schmidt coefficient for CO_3^{2-}, that is, $Sc=\nu/D_{CO3^{2-}}$ at $S_p = 35$ and in situ T, and $D_{CO3^{2-}}$ is the CO_3^{2-} diffusion coefficient from ref. 50. The geographical distribution of β is provided in *SI Appendix*, Fig. S3*C*. It should be noted that β is dependent on the temperature (*SI Appendix*, Fig. S4*C*), and, in contrast to the deep sea where the temperature is relatively constant (*SI Appendix*, Fig. S1*B*), significant variations can be encountered in warmer environments such as on carbonate platforms. Although studies such as ref. 51 have shown that there might have been a measurable change in bottom-water temperatures over the hydrographic period (late 1970s to today), accounting for it would have a very small impact on our results, given that these changes are currently limited to a few tenths of a degree Celsius (51).

Finally, we provide a 1° × 1° global model of the DBL thicknesses (Z_{DBL}) at the SWI, obtained by dividing $D_{CO_3^{2-}}$ (at $S_P = 35$ and in situ T) by β, in *SI Appendix*, Fig. S3*B*. This model can be used to estimate solute exchange at the SWI and is available on the NOAA Ocean Carbon Data System website, https://www.nodc.noaa.gov/ocads/oceans/.

Note that other empirical laws estimating β as function of Sc and u^*, similar to Eq. **9**, can be found in the literature (52–55). In *SI Appendix*, Fig. S4*B*, we provide a comparison of the DBL thickness as a function of the shear velocity (u^*) for $T = 2$ °C and $S_p = 35$ from various studies. *SI Appendix*, Fig. S4 *D–F* shows the range of bottom-current velocities, shear velocities, DBL thicknesses, and CO_3^{2-} mass transfer coefficients encountered at the seafloor. In addition, we represent in *SI Appendix*, Fig. S4*B* the DBL thicknesses observed in ref. 19 based on the dissolution of alabaster plates deployed at the seafloor, as a function of the shear velocities from current-meter measurements or skin friction probes (19).

Sediment-Side Mass Transfer Coefficient (k_s). Values for k_s have been obtained from experiments on the dissolution of $CaCO_3$ beds, as reported in refs. 12 and 56. Based on ref. 12, whose results are statistically similar to those from ref. 56,

$$k_s\approx(326.9\pm39.5\text{ m a}^{-1})X_{\text{calcite}}{}^{0.5}, \quad [10]$$

at 25 °C, where X_{calcite} is the calcite content in surficial sediments from the 1° × 1° distribution model in *SI Appendix*, Fig. S2*A*. The sediment-side mass transfer coefficients were subsequently adjusted from the laboratory temperature to the deep-seafloor temperature ($T = 2$ °C) by assuming maximum activation energy for calcite dissolution in seawater of 50 kJ·mol^{-1}, following the arguments presented in ref. 11. The distribution of k_S is shown in *SI Appendix*, Fig. S2*B*.

We provide a comparison of in situ k_S and β in *SI Appendix*, Fig. S5, where the blue end of the color bar represents a strongly water-side transport-controlled calcite dissolution reaction, while the red end stands for a strongly sediment-side controlled reaction. As it can be seen in *SI Appendix*, Fig. S5, calcite dissolution over most (72%) of the seafloor is water-side transport-controlled, except for areas covered by calcite-depleted sediments, where the reaction rate is limited by internal processes such as porewater diffusion or processes occurring at the surface of the calcite grains, thus independent of bottom-water hydrodynamics (see the discussion in *SI Appendix* for further details).

CCD and Calcite Downward Flux at the CCD (F). The calcite content data in surficial sediments (X_{calcite}) from the dbSEABED database were used to estimate the CCD in each basin, as defined in *SI Appendix*, Fig. S6, excluding the Arctic and Southern Oceans (below 60 °S), as well as continental shelves and near-shore areas. As mentioned in the Introduction, the CCD is operationally defined as the depth where the $CaCO_3$ content falls below 10%. Thus, for each basin, we selected the data points for which X_{calcite} is equal to 0.10 ± 0.03 (or 10 ± 3%) and computed the arithmetic average of the seafloor depths associated with these measurements. These depths constitute our CCD estimates for each basin and are assumed to be representative of preindustrial conditions. The CCD for each basin is reported along with the associated uncertainty and number of measurement used in *SI Appendix*, Table S1.

At the CCD, by definition, the calcite sinking rate is equal to its dissolution rate. Thus, the calcite downward flux at the CCD level (F) was computed from the estimated preindustrial CCD and GLODAPv2.2016b data, per the following:

$$F=\frac{K_{sp}{}^*k^*}{[\text{Ca}^{2+}]}\exp\left(\text{CCD}\frac{\rho g}{p_c}\right)-k^*\left[CO_3^{2-}\right]_{\text{SW}}^{p-i}, \quad [11]$$

where p_c is a characteristic pressure (2) set to 511 atm, ρ is the mean density of seawater, g is the mean gravitational acceleration on Earth, and $\left[CO_3^{2-}\right]_{\text{SW}}^{p-i}$ is the preindustrial bottom-water CO_3^{2-} concentration.

Calcite Dissolution Rate Calculation. For preindustrial conditions, the dissolution rate at the seafloor between the CSD and the CCD is given by the following:

$$r=k^*\left(\left[CO_3^{2-}\right]_{\text{eq}}-\left[CO_3^{2-}\right]_{\text{SW}}\right), \quad [12]$$

which is Eq. **2** of the text. For the seafloor located below the CCD, all $CaCO_3$ arriving at the seafloor (F) dissolves, that is,

$$r=F, \quad [13]$$

and these two latter equations account for all of the benthic dissolution.

With added anthropogenic dissolution, Eq. **12** still accounts for dissolution between the CSD and the CCD, both of which may now have been migrated

upward, and Eq. **13** still accounts for dissolution below the snowline, which remained in place. To account for dissolution between the snowline and the CCD, which have now separated as a result of anthropogenic CO_2 intrusion in the deep ocean, all $CaCO_3$ settling between these depths now dissolves at the seafloor (and in the water column). In addition, previously deposited $CaCO_3$ will dissolve as well. We account for these two sources by setting

$$r = F + k^*\left(\left[CO_3^{2-}\right]_{eq} - \left[CO_3^{2-}\right]_{SW}\right). \quad [14]$$

This assumes that dissolution has not been sufficient to deplete $CaCO_3$ in the sediment.

Statistical Treatment. SDs for GLODAPv2 variables (shown in *SI Appendix*, Fig. S1) were computed as the sum of the observational errors reported in ref. 57 and the mapping interpolation errors from ref. 26. The SD on the average CCD values are reported along with the number of measurements used for each estimate. SDs for $[CO_3^{2-}]_{SW}$, $\Delta[CO_3^{2-}]_{SW}$, r, Δr, and F were computed following the standard rules of error propagation, as described in *SI Appendix*, Table S2. Because r was computed using Eq. **12**, Eq. **13**, or Eq. **14**, depending on the position of the sediment relative to the preindustrial and current CCDs, σ_r was computed using three different equations, reported in *SI Appendix*, Table S2. No uncertainty was considered for r (i.e., σ_r was set to zero) at locations where calcite dissolution is thermodynamically impossible, that is, when $([CO_3^{2-}]_{SW} + \sigma_{[CO_3^{2-}]_{SW}}) > [CO_3^{2-}]_{eq}$.

ACKNOWLEDGMENTS. We thank all who contributed to the creation of GLODAPv2. We also thank John H. Trowbridge and the two anonymous reviewers for valuable discussions and criticism. This research was funded by Natural Sciences and Engineering Research Council of Canada Discovery Grants (to A.M. and B.P.B.). D.S.T. and B.K.A.'s contributions to this study were funded by the US National Science Foundation (NSF) Grant OCE-0960820, and R.M.K. was funded by NSF Grant PLR-1425989. O.S. also acknowledges the Department of Earth and Planetary Sciences at McGill University for financial support during his residency in the graduate program.

1. Montenegro A, Brovkin V, Eby M, Archer D, Weaver AJ (2007) Long term fate of anthropogenic carbon. *Geophys Res Lett* 34:L19707.
2. Boudreau BP, Middelburg JJ, Meysman FJR (2010) Carbonate compensation dynamics. *Geophys Res Lett* 37:L03603.
3. Zachos JC, et al. (2005) Rapid acidification of the ocean during the Paleocene–Eocene thermal maximum. *Science* 308:1611–1615.
4. Zeebe RE, Zachos JC, Dickens GR (2009) Carbon dioxide forcing alone insufficient to explain Paleocene–Eocene thermal maximum warming. *Nat Geosci* 2:576–580.
5. Cui Y, et al. (2011) Slow release of fossil carbon during the Palaeocene–Eocene thermal maximum. *Nat Geosci* 4:481–485.
6. Archer D (2005) Fate of fossil fuel CO_2 in geologic time. *J Geophys Res* 110:C09S05.
7. Boudreau BP, Middelburg JJ, Hofmann AF, Meysman FJR (2010) Ongoing transients in carbonate compensation. *Global Biogeochem Cycles* 24:GB4010.
8. Feely RA, et al. (2004) Impact of anthropogenic CO_2 on the $CaCO_3$ system in the oceans. *Science* 305:362–366.
9. Ríos AF, et al. (2015) Decadal acidification in the water masses of the Atlantic Ocean. *Proc Natl Acad Sci USA* 112:9950–9955.
10. Perez FF, et al. (2018) Meridional overturning circulation conveys fast acidification to the deep Atlantic Ocean. *Nature* 554:515–518.
11. Boudreau BP (2013) Carbonate dissolution rates at the deep ocean floor. *Geophys Res Lett* 40:744–748.
12. Sulpis O, Lix C, Mucci A, Boudreau BP (2017) Calcite dissolution kinetics at the sediment–water interface in natural seawater. *Mar Chem* 195:70–83.
13. Boudreau BP, Jørgensen BB (2001) *The Benthic Boundary Layer* (Oxford Univ Press, Oxford).
14. Waters CN, et al. (2016) The Anthropocene is functionally and stratigraphically distinct from the Holocene. *Science* 351:aad2622.
15. Jenkins CJ (1997) Building offshore soils databases. *Sea Technol* 38:25–28.
16. Goff JA, Jenkins CJ, Williams SJ (2008) Seabed mapping and characterization of sediment variability using the usSEABED data base. *Cont Shelf Res* 28:614–633.
17. Archer D, Emerson S, Smith SR (1989) Direct measurement of the diffusive sublayer at the deep sea floor using oxygen microelectrodes. *Nature* 340:623–626.
18. Gundersen JK, Jørgensen BB (1990) Microstructure of diffusive boundary layers and the oxygen uptake of the sea floor. *Nature* 345:604–607.
19. Santschi PH, Anderson RF, Fleisher MQ, Bowles W (1991) Measurements of diffusive sublayer thicknesses in the ocean by alabaster dissolution, and their implications for the measurements of benthic fluxes. *J Geophys Res* 96:10641–10657.
20. Boudreau BP, Luo Y, Meysman FJR, Middelburg JJ, Dickens GR (2015) Gas hydrate dissociation prolongs acidification of the Anthropocene oceans. *Geophys Res Lett* 42:9337–9344A.
21. Fukuda SY, Suzuki Y, Shiraiwa Y (2014) Difference in physiological responses of growth, photosynthesis and calcification of the coccolithophore *Emiliania huxleyi* to acidification by acid and CO_2 enrichment. *Photosynth Res* 121:299–309.
22. Maugendre L, et al. (2017) No detectable effect of ocean acidification on plankton metabolism in the NW oligotrophic Mediterranean Sea: Results from two mesocosm studies. *Estuar Coast Shelf Sci* 186:89–99.
23. Pinsonneault AJ, Matthews HD, Galbraith ED, Schmittner A (2012) Calcium carbonate production response to future ocean warming and acidification. *Biogeosciences* 9:2351–2364.
24. Wootton JT, Pfister CA, Forester JD (2008) Dynamic patterns and ecological impacts of declining ocean pH in a high-resolution multi-year dataset. *Proc Natl Acad Sci USA* 105:18848–18853.
25. Gibbs SJ, Stoll HM, Bown PR, Bralower TJ (2010) Ocean acidification and surface water carbonate production across the Paleocene–Eocene thermal maximum. *Earth Planet Sci Lett* 295:583–592.
26. Lauvset SK, et al. (2016) A new global interior ocean mapped climatology: The 1° × 1° GLODAP version 2. *Earth Syst Sci Data* 8:325–340.
27. Khatiwala S, Primeau F, Hall T (2009) Reconstruction of the history of anthropogenic CO_2 concentrations in the ocean. *Nature* 462:346–349.
28. Archer D, Kheshgi H, Maier-Reimer E (1998) Dynamics of fossil fuel CO_2 neutralization by marine $CaCO_3$. *Global Biogeochem Cycles* 12:259–276.
29. Berelson WM, et al. (2007) Relating estimates of $CaCO_3$ production, export, and dissolution in the water column to measurements of $CaCO_3$ rain into sediment traps and dissolution on the sea floor: A revised global carbonate budget. *Global Biogeochem Cycles* 21:GB1024.
30. Battaglia G, Steinacher M, Joos F (2016) A probabilistic assessment of calcium carbonate export and dissolution in the modern ocean. *Biogeosciences* 13:2823–2848.
31. Smith SV, Mackenzie FT (2016) The role of $CaCO_3$ reactions in the contemporary oceanic CO_2 cycle. *Aquat Geochem* 22:153–175.
32. Doney SC, Fabry VJ, Feely RA, Kleypas JA (2009) Ocean acidification: The other CO_2 problem. *Annu Rev Mar Sci* 1:169–192.
33. Riebesell U, Körtzinger A, Oschlies A (2009) Sensitivities of marine carbon fluxes to ocean change. *Proc Natl Acad Sci USA* 106:20602–20609.
34. Smith HEK, et al. (2012) Predominance of heavily calcified coccolithophores at low $CaCO_3$ saturation during winter in the Bay of Biscay. *Proc Natl Acad Sci USA* 109:8845–8849.
35. Lewis E, Wallace DWR (1998) *Program Developed for CO_2 System Calculations* (Carbon Dioxide Information Analysis Center, Oak Ridge National Laboratory, US Department of Energy, Oak Ridge, TN), ORNL/CDIAC-105.
36. van Heuven S, Pierrot D, Rae JWB, Lewis E, Wallace DWR (2011) *MATLAB Program Developed for CO_2 System Calculations* (Carbon Dioxide Information Analysis Center, Oak Ridge National Laboratory, U.S. Department of Energy, Oak Ridge, TN), ORNL/CDIAC-105b.
37. Key RM, et al. (2015) *Global Ocean Data Analysis Project, Version 2 (GLODAPv2)* (Carbon Dioxide Information Analysis Center, Oak Ridge National Laboratory, US Department of Energy, Oak Ridge, TN), ORNL/CDIAC-162, NDP-P093.
38. Carter BR, Toggweiler JR, Key RM, Sarmiento JL (2014) Processes determining the marine alkalinity and calcium carbonate saturation state distributions. *Biogeosciences* 11:7349–7362.
39. Riley JP, Tongudai M (1967) The major cation/chlorinity ratios in sea water. *Chem Geol* 2:263–269.
40. Mucci A (1983) The solubility of calcite and aragonite in seawater at various salinities, temperatures and one atmosphere total pressure. *Am J Sci* 283:780–799.
41. Weatherall P, et al. (2015) A new digital bathymetric model of the world's oceans. *Earth Space Sci* 2:331–345.
42. Takahashi T, et al. (2002) Global sea–air CO_2 flux based on climatological surface ocean pCO_2, and seasonal biological and temperature effects. *Deep Sea Res Part II* 49:1601–1622.
43. Li Y-H, Gregory S (1974) Diffusion of ions in sea water and in deep-sea sediments. *Geochim Cosmochim Acta* 38:703–714.
44. Trossman DS, et al. (2016) Impact of topographic internal lee wave drag on an eddying global ocean model. *Ocean Model* 97:109–128.
45. Timko PG, et al. (2013) Skill testing a three-dimensional global tide model to historical current meter records. *J Geophys Res Oceans* 118:6914–6933.
46. Monin AS, Yaglom AM (1971) *Statistical Fluid Dynamics* (MIT Press, Cambridge, MA), Vols I and II.
47. Armi L (1977) The dynamics of the bottom boundary layer of the deep ocean. *Elsevier Oceanogr Ser* 19:153–164.
48. Csanady GT (1967) On the "resistance law" of a turbulent Ekman layer. *J Atmos Sci* 24:467–471.
49. Schink D, Guinasso N (1977) Modelling the influence of bioturbation and other processes on calcium carbonate dissolution at the sea floor. *The Fate of Fossil Fuel CO_2 in the Oceans*, eds Andersen NR, Malahoff A (Plenum Press, New York), pp 375–400.
50. Zeebe RE (2011) On the molecular diffusion coefficients of dissolved, and their dependence on isotopic mass. *Geochim Cosmochim Acta* 75:2483–2498.
51. Purkey SG, Johnson GC (2013) Antarctic bottom water warming and freshening: Contributions to sea level rise, ocean freshwater budgets, and global heat gain. *J Clim* 26:6105–6122.
52. Steinberger N, Hondzo M (1999) Diffusional mass transfer at sediment-water interface. *J Environ Eng* 125:192–200.
53. Deissler RG (1954) *Analysis of Turbulent Heat Transfer, Mass Transfer, and Friction in Smooth Tubes at High Prandtl and Schmidt Numbers. National Advisory Commitee Aerodynamics* (US Government Printing Office, Washington, DC), Technical Note 3145.
54. Shaw DA, Hanratty TJ (1977) Turbulent mass transfer rates to a wall for large Schmidt numbers. *AIChE J* 23:28–37.
55. Wood PE, Petty CA (1983) New model for turbulent mass transfer near a rigid interface. *AIChE J* 29:164–167.
56. Keir RS (1983) Variation in the carbonate reactivity of deep-sea sediments: Determination from flux experiments. *Deep Sea Res Part A* 30:279–296.
57. Olsen A, et al. (2016) The global ocean data analysis project version 2 (GLODAPv2)—an internally consistent data product for the world ocean. *Earth Syst Sci Data* 8:297–323.